

times (2400 to 13,900 years), an approximate flux of BC per year to the world's oceans of 8.4×10^{17} μmol (9) and an average deep ocean DOC concentration of 39 μM (29) we calculate that BC could be 4 to 22% of the total deep ocean DOC pool.

Within this calculation are a number of first-order approximations about BC in the oceans. Among them are the assumptions that (i) suspended BC resides only in the DOC pool and not the POC pool; (ii) oceanic BC has one homogeneous age; (iii) river inputs of BC to remote sediments are not significant; and (iv) BC (and DOC) removal processes are similar between oceans. All of these approximations are reasonable given the available information; however, it is likely that they simplify the actual environmental processes. Small changes in each of these variables could result in site-to-site variability in the estimated residence time of BC in the water column, variabilities such as those observed between our northeastern Pacific and Southern Ocean sites (2400 to 5400 years and 13,900 years, respectively). For example, if the largest BC particles are removed closer to shore, the age difference between BC and non-BC SOC would be smaller closer to continents (providing one possible explanation for the difference between our Southern and Pacific ocean cores). Once the causes of these site-to-site differences are better understood, it may be possible to use sedimentary BC as a tracer of water column and sedimentary carbon cycle processes.

REFERENCES AND NOTES

1. T. A. J. Kuhlbusch and P. J. Crutzen, *Global Biogeochem. Cyc.* **9**, 491 (1995).
2. J. E. Penner, H. Eddleman, T. Novakov, *Atmos. Environ.* **27A**, 1277 (1993).
3. J. A. Ogren and R. J. Charlson, *Tellus* **35B**, 241 (1983).
4. W. S. Wolbach, R. S. Lewis, E. Anders, *Science* **230**, 167 (1985).
5. J. R. Herring, in *The Carbon Cycle and Atmospheric CO₂: Natural Variations, Archaeal to Present*, E. T. Sundquist and W. S. Broecker, Eds. (1985), pp. 419–442.
6. J. M. Smith, J. J. Griffin, E. D. Goldberg, *Nature* **241**, 268 (1973).
7. J. A. Rau and M. A. K. Khalil, *Atmos. Environ.* **27A**, 1297 (1993).
8. M. O. Andreae, T. W. Andreae, R. J. Ferek, H. Raedonck, *Sci. Tot. Environ.* **36**, 73 (1984).
9. D. O. Suman, T. A. J. Kuhlbusch, B. Lim, in *Sediment Records of Biomass Burning and Global Change*, J. S. Clark, H. Cachier, J. G. Goldammer, B. J. Stocks, Eds. (Springer-Verlag, Berlin, 1997), pp. 271–293.
10. W. S. Wolbach and E. Anders, *Geochim. Cosmochim. Acta* **53**, 1637 (1989).
11. J. I. Hedges and R. G. Keil, *Mar. Chem.* **49**, 81 (1995).
12. E. D. Goldberg, *Black Carbon in the Environment* (Wiley, New York, 1985).
13. D. O. Suman, thesis, University of California at San Diego (1983).
14. D. J. Verardo and W. F. Ruddiman, *Geology* **24**, 855 (1996).
15. P. M. Williams and E. R. M. Druffel, *Nature* **330**, 246 (1987).
16. S. E. Trumbore and E. R. M. Druffel, in *Role of Non-living Organic Matter in the Earth's Carbon Cycle*, R. G. Zepp and C. Sonntag, Eds. (Wiley, New York, 1995), pp. 7–22.
17. E. R. M. Druffel and C. A. Masiello, unpublished data.
18. K. L. Smith Jr., R. S. Kaufmann, R. J. Baldwin, *Limnol. Oceanogr.* **39**, 1101 (1994).
19. We demineralized 20 g of dried sediment in alternating solutions of 6 N HCl and 50% HF, and then oxidized the remaining material for 400 hours at 23°C in 0.25 M Cr₂O₇²⁻/2 M H₂SO₄. Between each extraction step, the samples were rinsed four to six times with high-purity water. After extraction, BC was dried, weighed, and combusted to CO₂, reduced to graphite with H₂ gas, and then measured for radiocarbon at the Center for Accelerator Mass Spectrometry of the Lawrence Livermore National Laboratories (CAMS LLNL).
20. The non-BC SOC fraction modern (FM) was calculated by mass balance by solving the equation $FM_{SOC\ total} = (FM_{BC} \times \text{fraction BC}) + (FM_{non-BC\ SOC} \times \text{fraction non-BC SOC})$ for the variable $FM_{non-BC\ SOC}$.
21. J. E. Bauer, C. E. Reimers, E. R. M. Druffel, P. M. Williams, *Nature* **373**, 686 (1995).
22. W. S. Reeburgh, *Bull. Eco. Soc. Am.* **78**, 260 (1997).
23. M. Stuiver, G. W. Pearson, T. Braziunas, *Radiocarbon* **28**, 980 (1986).
24. M. P. Bacon and R. F. Anderson, *J. Geophys. Res.* **87**, 2045 (1982); W. G. Deuser, P. G. Brewer, T. D. Jickells, R. F. Commeau, *Science* **219**, 388 (1982).
25. R. M. Sherrell, M. P. Field, Y. Gao, K. L. Smith, *Deep Sea Res. II*, in press.
26. J. I. Hedges and D. C. Mann, *Geochim. Cosmochim. Acta* **43**, 1809 (1979).
27. J. I. Hedges, R. G. Keil, R. Benner, *Org. Geochem.* **V27**, 195 (1997).
28. H. Cachier, P. Buat-Menard, M. Fontugne, J. Rancher, *J. Atmos. Chem.* **3**, 469 (1985).
29. E. R. M. Druffel, P. M. Williams, J. E. Bauer, J. Ertel, *J. Geophys. Res.* **97**, 15639 (1992).
30. R. J. Blong and R. Gillespie, *Nature* **271**, 739 (1978).
31. C. Lioussse, J. E. Penner, C. Chuang, J. J. Walton, H. Eddleman, *J. Geophys. Res.* **101**, 19411 (1996).
32. W. F. Cooke and J. J. N. Wilson, *ibid.*, p. 19395.
33. S. G. Jennings *et al.*, *ibid.*, p. 19447.
34. M. O. Andreae, *Science* **220**, 1148 (1983).
35. E. R. M. Druffel, J. E. Bauer, P. M. Williams, S. Griffin, D. Wolgast, *J. Geophys. Res.* **101**, 20543 (1996).
36. W. J. Cai, C. E. Reimers, T. Shaw, *Geochim. Cosmochim. Acta* **59**, 497 (1995).
37. We thank S. Griffin for guidance in the laboratory; J. Southon and M. Kashgarian for AMS measurements at CAMS LLNL; S. Trumbore and S. Zheng for shared resources; J. Bauer and colleagues, A. Pearson, and officers and crew of R/V *New Horizon* and R/V *Melville* for shipboard assistance; K. Smith and colleagues for shared ship time; and J. Bauer, L. Keigwin, S. Trumbore, W. Reeburgh, A. Alldredge, J. Hedges, H. Tucker, and two anonymous reviewers for comments. We acknowledge funding from the Chemical Oceanography program of NSF through grants OCE-9314691 and OCE-9417391.

2 March 1998; accepted 13 April 1998

Elasticity of Single-Crystal MgO to 8 Gigapascals and 1600 Kelvin

Ganglin Chen,* Robert C. Liebermann,† Donald J. Weidner

The cross pressure (P) and temperature (T) dependence of the elastic moduli (C_{ij}) of single-crystal samples of periclase (MgO) from acoustic wave travel times was measured with ultrasonic interferometry: $\partial^2 C_{11}/\partial P \partial T = (-1.3 \pm 0.4) \times 10^{-3}$ per kelvin; $\partial^2 C_{110}/\partial P \partial T = (1.7 \pm 0.7) \times 10^{-3}$ per kelvin; and $\partial^2 C_{44}/\partial P \partial T = (-0.2 \pm 0.3) \times 10^{-3}$ per kelvin. The elastic anisotropy of MgO decreases with increasing pressure at ambient temperature, but then increases as temperature is increased at high pressure. An assumption of zero cross pressure and temperature derivatives for the elastic moduli underestimates the elastic anisotropy and overestimates the acoustic velocities of MgO at the extrapolated high-pressure and high-temperature conditions of Earth's mantle.

Periclase has the cubic rock salt (B1) structure. It has traditionally been regarded as a standard solid for testing new experimental techniques developed for elasticity measurements (1–5) and for theoretical modeling and analyses of thermoelastic properties of solids at elevated pressure and temperature (6–8). It is an important mineral in geophysics because mineralogical models of Earth's lower mantle contain magnesiowüstite, (Mg_x, Fe_{1-x})O (9), on the basis of high

pressure–high temperature phase equilibrium experiments (10). Its availability and stability over a wide range in the pressure–temperature space have prompted its use as a pressure standard in high pressure–high temperature x-ray diffraction experiments in diamond anvil cells and multianvil apparatus (11, 12).

Although the elastic properties of MgO have been the subject of numerous experimental and theoretical investigations over the past 30 years, direct measurements of the acoustic velocities with the techniques of physical acoustics have been made primarily at high pressure (≤ 8 GPa) but ambient temperature (2–4), or at high temperature (≤ 1800 K) but ambient pressure (5). A previous effort to map the elasticity of this mineral at simultaneous elevated pressures and temperatures covered the range

G. Chen, Center for High Pressure Research and Mineral Physics Institute, State University of New York (SUNY), Stony Brook, NY 11794, USA.

R. C. Liebermann and D. J. Weidner, Center for High Pressure Research and Department of Geosciences, SUNY, Stony Brook, NY 11794, USA.

*Present address: ST541 EPR, Exxon Production Research Company, Post Office Box 2189, Houston, TX 77252-2189, USA.

†To whom correspondence should be addressed.

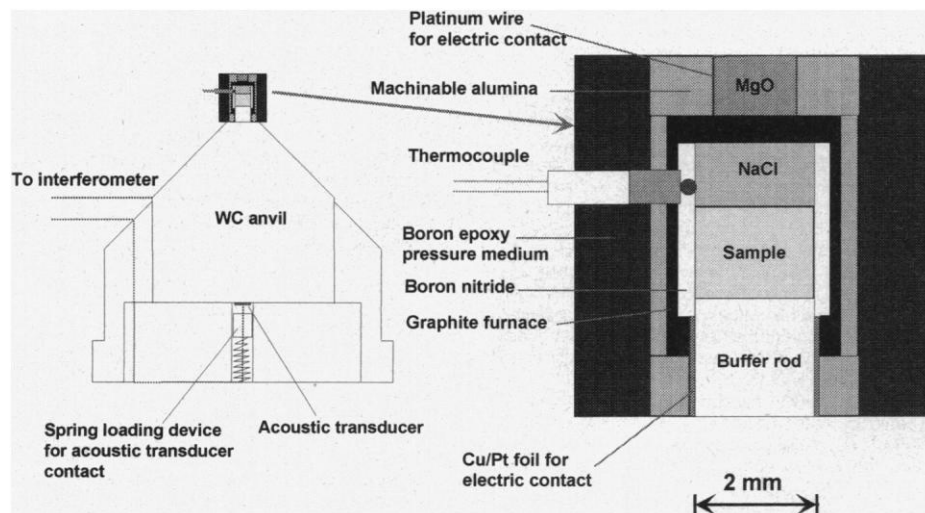


Fig. 1. Acoustic transducer tungsten carbide anvil setup (left) and the sample cell assembly (right) for the simultaneous ultrasonic and x-ray experiment at high pressure and high temperature.

up to 0.8 GPa and 800 K (1). For such a highly incompressible solid, this restricted range of experimental conditions has not allowed an unambiguous determination of the cross pressure and temperature dependence of the elastic moduli or the acoustic velocities.

Progress has been made in several laboratories to develop techniques for performing acoustic measurements in multianvil apparatus at the pressure and temperature conditions approaching those of the transition zone (pressure $P = 13$ to 23 GPa, temperature $T > 1500$ K) of Earth's mantle, with both single-crystal samples (13) and polycrystalline samples (14). Recently, we adapted these techniques to a DIA-type, cubic anvil, high-pressure apparatus (SAM85) installed on the superconducting wiggler beamline (X17B1) at the National Synchrotron Light Source of the Brookhaven National Laboratory (15). X-ray spectra of the sample and the NaCl pressure medium that surrounds it can be monitored continuously; the former provides pressure-volume-temperature (PVT) data to complement the velocity measurements and the latter the pressure standard. These developments enable in situ ultrasonic and x-ray measurements to be performed simultaneously at high pressure and temperature (16). Data for polycrystalline alumina obtained with this apparatus (SAM85 with x-rays) agree with those obtained on a uniaxial, split-cylinder, high-pressure apparatus (USCA-1000) using discrete pressure calibration points of Bi and ZnTe (16, 17); these data confirm the suitability of Bi and ZnTe as pressure indicators in the acoustic experiments and lend additional credibility to the ultrasonic data obtained with the USCA-1000 (13, 14).

Here we present data on the elasticity of single-crystal MgO measured in SAM85 to 8 GPa and 1600 K with ultrasonic interferometry. The acoustic piezoelectric transducer-tungsten carbide (WC) anvil arrangement and the high-temperature cell assembly used in SAM85 have LiNbO₃ transducers (40 MHz, 36° Y-cut for compressional waves and 41° X-cut for shear waves) that are mounted onto the back side of the WC anvil (Toshiba grade F) with a high-temperature epoxy and connected to the interferometer by coaxial cables (Fig. 1). The WC anvil serves as an acoustic buffer rod to transmit the high-frequency signal (20 to 70 MHz) into the cell assembly (18). The single-crystal sample is centered within the cubic cell assembly and is surrounded by a boron nitride sleeve. The acoustic signal is transmitted into the sample through another buffer rod of fused-silica glass. The NaCl disc serves two important purposes: it provides (i) a pseudo hydrostatic pressure environment for the sample (15), and (ii) a pressure standard at room temperature and high temperature in the Decker equation of state (19).

Acoustic travel times corresponding to three elastic modes were measured (20): compressional modes for the [100] and [110] directions and a shear mode for [100]. We converted the acoustic travel times to elastic moduli using the high-precision x-ray diffraction volume data of MgO obtained by Utsumi *et al.* (11) in the same high-pressure apparatus over a comparable pressure and temperature range, thus providing data for the three elastic moduli C_{11} , C_{44} , and C_{110} with uncertainties of about 1%. The modulus data at ambient temperature agree with the results of Jackson and Niesler (2) obtained in a gas pressure vessel to 3 GPa (Fig. 2). With the high-precision modulus values

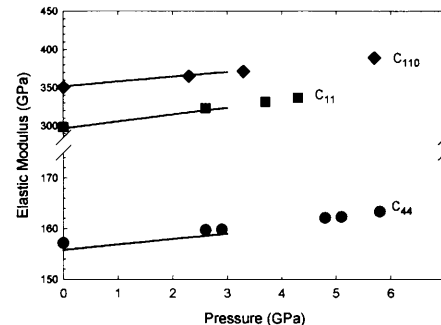


Fig. 2. Elastic moduli of MgO versus pressure at ambient temperature ($C_{11} = \rho V_{p[100]}^2$, $C_{44} = \rho V_{s[100]}^2$, and $C_{110} = \rho V_{p[110]}^2$, where ρ is density, V_p is the velocity of the compressional wave, and V_s is the velocity of the shear wave). The symbols are from this study; uncertainties in the moduli are about the size of the symbols. The three solid curves are results obtained by Jackson and Niesler (2) in a gas pressure vessel.

along the pressure (acoustic data, this study) and temperature (5) axes and the wide P-T coverage of the present ultrasonic data, the cross pressure and temperature derivatives of the elastic moduli for MgO were calculated (Table 1) (21). Our results indicate that the effect of cross pressure and temperature dependence on the behavior of C_{11} and C_{44} is different. Whereas the cross-derivative ($\partial^2 C_{11} / \partial P \partial T$) [that is, the temperature derivative of ($\partial C_{11} / \partial P$)_T] is about $10^{-3}/K$, the cross-derivative for the C_{44} mode ($\partial^2 C_{44} / \partial P \partial T$) is an order of magnitude smaller in absolute value, and a value different from zero is not resolvable by our data. Furthermore, the effect of cross pressure and temperature dependence on the bulk modulus is also about $10^{-3}/K$, in agreement with the earlier suggestions derived from experimental data (22), but in marked contrast to the conclusions drawn when the cross derivatives of the bulk modulus were computed from thermodynamic relations

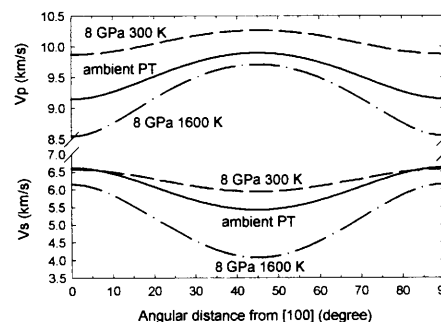
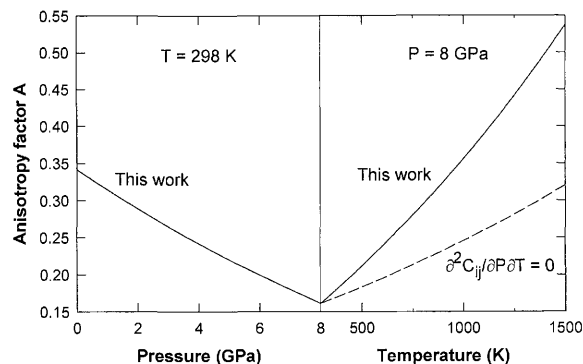


Fig. 3. Compressional (V_p) and shear wave (V_s) velocities as functions of angular distance from [100] orientation in the (001) plane at different pressure and temperature conditions: solid curve, ambient condition (1 bar, 300 K); dashed curve, 8 GPa and 300 K; and dashed-dot curve, 8 GPa and 1600 K.

Table 1. Cross pressure and temperature derivatives of elastic moduli of MgO (19) (all in the unit of $10^{-3}/\text{K}$; $C_{11} = \rho V_{p[100]}^2$, $C_{44} = \rho V_{s[100]}^2$, $C_{110} = \rho V_{p[110]}^2$, and adiabatic bulk modulus $K_S = (C_{11} + 2C_{12})/3$) from this study (to 8 GPa, 1600K) and earlier work of Spetzler (7) to 0.8 GPa and 800 K.

Study	$\partial^2 C_{11}/\partial P \partial T$	$\partial^2 C_{44}/\partial P \partial T$	$\partial^2 C_{110}/\partial P \partial T$	$\partial^2 K_S/\partial P \partial T$
This study	-1.3 (0.4)	-0.2 (0.3)	1.7 (0.7)	2.7 (1.1)
Spetzler (7)	-0.3 to 0.5	0 to 0.2	-0.1 to 1.0	-0.2 to 0.4

Fig. 4. Elastic anisotropy of MgO as functions of pressure and temperature. The solid curves are based on the modulus data from this study; the dashed curve on the right panel assumes zero cross pressure and temperature derivatives for the elastic moduli.



and lattice dynamics modeling (6, 23). When modeling the composition of Earth's lower mantle or formulating the equation of state of MgO at the high-pressure and high-temperature regime, one must take into account the effect of the cross pressure and temperature dependence on the acoustic velocities and elastic moduli of MgO. For example, neglect of these ($\partial^2 C_{ij}/\partial P \partial T$) terms leads to overestimates of 1.7% for the compressional (C_{11}) and 0.8% for the shear (C_{44}) velocities of MgO at $P = 10$ GPa and $T = 1300$ K.

Although the cubic MgO is optically isotropic, it exhibits a substantial elastic anisotropy at ambient pressure and temperature (Fig. 3). Increasing pressure at ambient temperature suppresses compressional wave and shear wave anisotropy. However, temperature has a dramatic and opposite effect on the elastic wave anisotropy for this cubic material. When temperature is increased to 1600 K at 8 GPa, the elastic wave anisotropy (both compressional and shear) becomes even stronger than at ambient conditions. Quantitatively, we characterize this anisotropy by the anisotropy factor [for example, (7)]: $A = 2(C_{44} - C_S)/C_{11}$, where $C_S = (C_{11} - C_{12})/2$. For isotropic elasticity, the two shear moduli C_{44} and C_S are equal and $A = 0$. Using our acoustic data, we calculated the evolution of A at high pressures and temperatures (Fig. 4). With increasing pressure at ambient temperature, A decreases and would vanish at about 19 GPa from extrapolation of our data. A similar trend is observed from extrapolating Jackson and Niesler's data (2) (21 GPa) and from the theoretical calculations by Karki et al. (7) (15 GPa); experimental evidence for such a transition was provided by Duffy et

al. (24). As temperature increases, our data show that the elastic anisotropy increases. At 8 GPa, the anisotropy factor A recovers to the value of ambient conditions by about 1000 K. An assumption of zero cross-derivatives (dashed curve) would significantly underestimate the temperature effect on the anisotropy at high pressure. Thus, at elevated pressure and temperature conditions, such as those typical of Earth's deep interior, MgO may remain distinctly anisotropic.

REFERENCES AND NOTES

- H. A. Spetzler, *J. Geophys. Res.* **75**, 2073 (1970).
- I. Jackson and H. Niesler, in *High-Pressure Research in Geophysics*, S. Akimoto and M. H. Manghnani, Eds. (Reidel, Boston, 1982), pp. 93-113.
- T. S. Duffy and T. J. Ahrens, *J. Geophys. Res.* **100**, 529 (1995); A. Chopelas, *Earth Planet. Sci. Lett.* **114**, 185 (1992); A. H. Shen et al., in *High-Pressure Research Properties of Earth and Planetary Materials*, M. H. Manghnani and T. Yagi, Eds. [American Geophysical Union (AGU), Washington, DC, 1998], pp. 71-77.
- A. Yoneda, *J. Phys. Earth* **38**, 19 (1990).
- D. G. Isaak, O. L. Anderson, T. Goto, *Phys. Chem. Mineral.* **16**, 704 (1989).
- D. G. Isaak, R. E. Cohen, M. J. Mehl, *J. Geophys. Res.* **95**, 7055 (1989).
- B. B. Karki et al., *Am. Mineral.* **82**, 51 (1997).
- K. Wang and R. R. Reeber, *Geophys. Res. Lett.* **22**, 1297 (1995); O. L. Anderson, in *Equations of State of Solids for Geophysics and Ceramic Science* (Oxford Univ. Press, New York, 1995), pp. 57-82.
- D. J. Weidner and E. Ito, in *High-Pressure Research in Mineral Physics*, M. H. Manghnani and Y. Syono, Eds. (AGU, Washington, DC, 1987), pp. 439-446; T. S. Duffy and D. L. Anderson, *J. Geophys. Res.* **94**, 1895 (1989); J. Ita and L. Stixrude, *ibid.* **97**, 6849 (1992).
- Y. Fei, H.-K. Mao, B. O. Mysen, *J. Geophys. Res.* **96**, 2157 (1991); E. Takahashi and E. Ito, in *High-Pressure Research in Mineral Physics*, M. H. Manghnani and Y. Syono, Eds. (AGU, Washington, DC, 1987), pp. 427-437.
- W. Utsumi, D. J. Weidner, R. C. Liebermann, in *High-Pressure Research Properties of Earth and Planetary Materials*, M. H. Manghnani and T. Yagi, Eds. (AGU,

- Washington, DC, 1998), pp. 327-333.
- J. C. Jamieson, J. N. Fritz, M. H. Manghnani, in (2), pp. 27-48.
- G. Chen, B. Li, R. C. Liebermann, *Science* **272**, 979 (1996).
- B. Li, I. Jackson, T. Gasparik, R. C. Liebermann, *Phys. Earth Planet. Inter.* **98**, 79 (1996); B. Li, G. Chen, G. D. Gwanmesia, R. C. Liebermann, in (1), pp. 41-61; R. Knoche, S. L. Webb, D. C. Rubie, in (1), pp. 119-128.
- D. J. Weidner et al., in *High-Pressure Research: Application to Earth and Planetary Sciences*, Y. Syono and M. H. Manghnani, Eds. (AGU, Washington, DC, 1992), pp. 13-17; M. T. Vaughan, in *Short Course Handbook on Experiments at High Pressure and Applications to the Earth's Mantle*, R. W. Luth, Ed. (Mineralogical Association of Canada, Ontario, 1993), pp. 95-131; Y. Wang, I. C. Getting, D. J. Weidner, M. T. Vaughan, in (1), pp. 35-39.
- R. C. Liebermann et al., *Eos* **77**, F672 (1996); R. C. Liebermann et al., *Rev. High Pressure Sci. Technol.*, in press.
- The pressure calibration points for Bi and ZnTe are the following: Bi, 2.5 GPa and 7.7 GPa; ZnTe, 9.6 GPa and 12.5 GPa [E. C. Lloyd, *Natl. Bur. Stand. Spec. Publ.* 326 (1971), pp. 1-3; M. Nomura, T. Nishizaka, Y. Hirata, N. Nakagiri, H. Fujiwara, *Jpn. J. Appl. Phys.* **21**, 936 (1982); K. Kusaba et al., *Pure Appl. Geophys.* **141**, 644 (1993)].
- The parallel electrode, piezoelectric acoustic transducer is housed in the hollow, hardened steel plate and is stress free; electric contact to the transducer is by a spring-loading device and is grounded by a 50-ohms resistor. The WC anvil serves as the first stage acoustic buffer rod. Glass is the choice for the second buffer rod because of the acoustic impedance contrast between the MgO sample and the buffer rod; the relatively low acoustic velocities of glass material also make time separation between the glass echo and the sample echo possible. Figure 1 shows the experimental setup and the sample cell assembly for the high pressure-high temperature acoustic travel time measurements. The transducer WC anvil, one of the six anvils used to generate high pressure in the DIA high-pressure apparatus (15), is shown in Fig. 1, left. The detail of the sample cell assembly is shown in Fig. 1, right. A second stage, fused-silica glass buffer rod is used to center the sample in the hot zone of the graphite furnace; the sample temperature was monitored actively throughout the experiment by a pair of tungsten-rhenium thermocouples. Sodium chloride powder is packed on the other end of the sample, serving as a pressure standard through simultaneous x-ray diffraction volume measurements of NaCl (19). The interface between the sample and NaCl reflects much of the acoustic energy because of the high acoustic impedance contrast, providing an ideal acoustic boundary for the ultrasonic stack (WC anvil, glass buffer rod, and sample). The low yielding strength of NaCl also provides a pseudo-hydrostatic environment for the sample, especially at elevated temperatures (15). Uncertainties in the pressure were estimated to be ~0.1 GPa (similar magnitude for the pressure gradient over a 1-mm sample length) at high pressures from the x-ray diffraction volume measurements of NaCl, assuming a typical pressure derivative of the travel time (t) on the order of $(1/t)(dt/dP) = 10^{-5}/\text{MPa}$; uncertainties in the travel time due to the uncertainties in pressures were $100 \times 10^{-5} = 0.1\%$. A double-thermocouple installation in the sample cell recorded a temperature gradient along the furnace axis of about 50 K/mm at 1000 K, assuming a typical temperature derivative of the travel time on the order of $(1/t)(dt/dT) = 10^{-5}/\text{K}$; uncertainties in the travel times due to the temperature gradient over 1 mm was $50 \times 10^{-5} = 5 \times 10^{-4} < 0.1\%$.
- D. L. Decker, *J. Appl. Phys.* **42**, 3239 (1971); F. Birch [*J. Geophys. Res.* **91**, 4949 (1986)] rederived the equation of state for NaCl. Our comparison of Birch's and Decker's results indicates that they only differ by 0.15 GPa at the maximum pressure reached in our study (8 GPa). The uncertainties (<0.2%) (18) introduced in the travel times are less than the mea-

surement precisions (0.5%) (20) in the travel times themselves.

20. Single-crystal samples of MgO (purity >99.9%) were oriented with x-ray diffraction method described in (13) to [100] and [110] orientations (better than 1°); the samples were cored, cut, and polished to cylinders of about 1.8 mm in diameter and 1.2 to 1.5 mm in length. The original sample lengths were measured to micrometers, that is, $\pm 1 \mu\text{m}$. Measurements of the sample travel time were achieved by overlapping the glass buffer rod echo and the sample echo and recording the amplitudes of the interference signal as a function of the frequency (from 20 to 70 MHz). Precision in the travel time measurements is about 2 ns or 0.5% for the sample used in this study. We used Pt (20 μm thick) and Au (2 μm thick) foils to couple the acoustic wave from the glass buffer rod to the sample. These metal foils alleviate the problems of the compressibility and thermal expansivity mismatches between the buffer and the sample, but they also introduce uncertainties in the acoustic travel time [(25); I. Jackson, H. Niesler, D. J. Weidner, *J. Geophys. Res.* **86**, 3736 (1981)]. Their effect on the travel times is calculated and removed with the algorithm detailed in (25). Redundant experiments were also performed with Pt foil and Au foil for the same elastic mode (C_{44});

after correcting for the effect of the bonds (Pt or Au foils), the sample travel times agree within the measurement uncertainties (2 ns).

21. In extracting the cross pressure-temperature derivatives of the elastic moduli ($\partial^2 C_{ij}/\partial P \partial T$), our modulus data at elevated P and T are fit by polynomials [$C_{ij} = C_{ij}^0 + (\partial C_{ij}/\partial P)P + (\partial C_{ij}/\partial T)T + (\partial^2 C_{ij}/\partial P \partial T)PT$] with the constraints of fixing the pressure derivatives ($\partial C_{ij}/\partial P$) at ambient temperature (from our high pressure-ambient temperature data) and the temperature derivatives ($\partial C_{ij}/\partial T$) at ambient pressure [from averaging the rectangular parallelepiped resonance (RPR) data (5)]. Such fits are mathematically robust because the boundary conditions (along the pressure and temperature axes) are well defined: the RPR method provides data if very high precision along the temperature axis, and the acoustic data along the pressure axis also have high precision [in light of their good agreement with the results obtained from the gas pressure vessel (Fig. 3)].
22. D. G. Isaak and E. K. Graham, *J. Geophys. Res.* **81**, 2483 (1976); G. Chen, A. Yoneda, I. C. Getting, H. A. Spetzler, *ibid.* **101**, 25 (1996).
23. D. G. Isaak, *Phys. Earth Planet. Inter.* **80**, 37 (1993).
24. T. S. Duffy, R. J. Hemly, H. K. Mao, *Phys. Rev. Lett.* **74**, 1371 (1995).

25. H. A. Spetzler, G. Chen, S. Whitehead, I. C. Getting, *Pure Appl. Geophys.* **141**, 341 (1993).

26. This work was carried out with the X17B1 beamline of the National Synchrotron Light Source (NSLS) of the Brookhaven National Laboratory. Y. Sinelnikov helped in carrying out the experiments. We thank all of the personnel who contributed to the execution of these ultrasonic experiments; J. B. Hastings and D. P. Siddons (NSLS) for their technical supports at the beamline; C. Koleda, P. Hoversen, H. Schay, B. Huebsch, B. Vitale, and K. Baldwin (SUNY, Stony Brook) for their support in machining cell parts and maintenance of the high-pressure and high-temperature apparatus; J. Chen and M. Vaughan (SUNY, Stony Brook) of the SAM85 operational team for their support in this new project; and Y. Wang (Consortium for Advanced Radiation Sources, Chicago) for valuable suggestions on designing the cell assembly. These high-pressure experiments were conducted with the joint support of SUNY and the NSF Science and Technology Center for High Pressure Research (CHIPR) under grant EAR89-20239 and by NSF grants to R.C.L. (EAR93-04502 and 96-14612). This is Mineral Physics Institute publication number 230.

2 March 1998; accepted 12 May 1998

The Influence of Vegetation-Atmosphere-Ocean Interaction on Climate During the Mid-Holocene

Andrey Ganopolski, Claudia Kubatzki,* Martin Claussen, Victor Brovkin, Vladimir Petoukhov

Simulations with a synchronously coupled atmosphere-ocean-vegetation model show that changes in vegetation cover during the mid-Holocene, some 6000 years ago, modify and amplify the climate system response to an enhanced seasonal cycle of solar insolation in the Northern Hemisphere both directly (primarily through the changes in surface albedo) and indirectly (through changes in oceanic temperature, sea-ice cover, and oceanic circulation). The model results indicate strong synergistic effects of changes in vegetation cover, ocean temperature, and sea ice at boreal latitudes, but in the subtropics, the atmosphere-vegetation feedback is most important. Moreover, a reduction of the thermohaline circulation in the Atlantic Ocean leads to a warming of the Southern Hemisphere.

demonstrated that some of the climatic differences might be explained by changes in ocean temperatures, but again, the simulations reveal only partial agreement with paleodata. We describe the strong synergistic effect of the response of atmosphere, ocean, and vegetation on the changed solar insolation conditions found in our coupled atmosphere-ocean-vegetation model.

We used a climate system model of intermediate complexity, CLIMBER (for CLIMATE and BiosphERE) (21, 22), to perform a set of consistent experiments with different model configurations from the atmosphere-only model to the coupled atmosphere-ocean-terrestrial vegetation model. CLIMBER does not employ any flux adjustment between the atmospheric and oceanic modules. The model has a coarse resolution of 10° in latitude and 51° in longitude. It encompasses a 2.5-dimensional dynamical-statistical atmosphere model; a multibasin, zonally averaged ocean model, including sea ice; and a terrestrial vegetation model (23). The latter simulates vegetation that is in equilibrium with climate. Vegetation cover is represented as a mixture of trees, grass, and desert (bare soil). The fraction of each is not a discrete, but a continuous function of growing degree days (sum of mean daily temperature for days with temperature above 0°C) and annual precipitation. Hence, in contrast to biome-type models, CLIMBER is able to describe changes in vegetation cover that can be interpreted as shifts in vegetation zones smaller than the spatial resolution of the model.

A control run was performed, using the fully coupled atmosphere-ocean-biosphere version of the model for characteristics of preindustrial climate (when the system was close to equilibrium)—in other words, modern solar insolation and a CO₂ concentra-

Numerous paleodata suggest that the climate of the mid-Holocene around 6 thousand years ago (ka) was quite different from that of today. Generally, the summer in many mid- to high-latitude regions of the Northern Hemisphere was warmer, and paleobotanic data indicate an expansion of boreal forests north of the modern tree line (1–6). In North Africa, paleoclimatological reconstructions (5, 7, 8) reveal a climate

wetter than today's. Moreover, it has been found (9, 10) that vegetation covered a substantial part of the Sahara during the mid-Holocene. Climate models have been used to examine how the changes in Earth's orbit result in the differences between the climate of today and that of 6 ka. Atmosphere models that use prescribed modern sea surface temperatures (SSTs), sea-ice distribution, and vegetation cover (11–14) seem to underestimate the amplitude of the observed climatic differences (2, 5). Sensitivity studies in which artificially prescribed changes in vegetation were introduced into climate models (2, 15, 16) suggest that positive feedbacks between climate and vegetation can be important in explaining the climate changes during the Holocene. Coupled atmosphere-vegetation models (17, 18) support this hypothesis. Recently, coupled atmosphere-ocean models (19, 20)

A. Ganopolski, C. Kubatzki, V. Brovkin, Potsdam-Institut für Klimafolgenforschung, Postfach 601203, D-14412 Potsdam, Germany.

M. Claussen, Potsdam-Institut für Klimafolgenforschung, Postfach 601203, D-14412 Potsdam, Germany and Institut für Meteorologie, FU Berlin, C.-H. Becker Weg 6-10, D-12165 Berlin, Germany.

V. Petoukhov, Potsdam-Institut für Klimafolgenforschung, Postfach 601203, D-14412 Potsdam, Germany and Oboukhov Institute for Atmospheric Physics, Pzhevsyky 3, 109017 Moscow, Russia.

*To whom correspondence should be addressed. E-mail: kubi@pik-potsdam.de